





A predictive microfluidic model of human glioblastoma to assess trafficking of blood–brain barrier-penetrant nanoparticles

Joelle P. Straehla^{a,b,c,1}, Cynthia Hajal^{d,1,2} , Hannah C. Safford^a, Giovanni S. Offeddu^e , Natalie Boehnke^a, Tamara G. Dacoba^{a,f}, Jeffrey Wyckoff^g, Roger D. Kamm^{d,e,3,4} , and Paula T. Hammond^{a,g,3,4}

Contributed by Paula T. Hammond; received October 11, 2021; accepted March 15, 2022; reviewed by Brendan Harley, Samir Mitragotri, and Ronit Satchi-Fainaro

The blood–brain barrier represents a significant challenge for the treatment of high-grade gliomas, and our understanding of drug transport across this critical biointerface remains limited. To advance preclinical therapeutic development for gliomas, there is an urgent need for predictive *in vitro* models with realistic blood–brain-barrier vasculature. Here, we report a vascularized human glioblastoma multiforme (GBM) model in a microfluidic device that accurately recapitulates brain tumor vasculature with self-assembled endothelial cells, astrocytes, and pericytes to investigate the transport of targeted nanotherapeutics across the blood–brain barrier and into GBM cells. Using modular layer-by-layer assembly, we functionalized the surface of nanoparticles with GBM-targeting motifs to improve trafficking to tumors. We directly compared nanoparticle transport in our *in vitro* platform with transport across mouse brain capillaries using intravital imaging, validating the ability of the platform to model *in vivo* blood–brain-barrier transport. We investigated the therapeutic potential of functionalized nanoparticles by encapsulating cisplatin and showed improved efficacy of these GBM-targeted nanoparticles both *in vitro* and in an *in vivo* orthotopic xenograft model. Our vascularized GBM model represents a significant biomaterials advance, enabling in-depth investigation of brain tumor vasculature and accelerating the development of targeted nanotherapeutics.

glioblastoma | microfluidic | nanoparticle | blood–brain barrier | drug delivery

High-grade gliomas are the most common primary malignant brain tumors in adults (1). These include grade IV astrocytomas, commonly known as glioblastoma multiforme (GBM), which account for more than 50% of all primary brain cancers and have dismal prognoses, with a 5-y survival rate of less than 5% (2). Due to their infiltrative growth into the healthy brain tissue, surgery often fails to eradicate all tumor cells (3). While chemotherapy and radiation modestly improve median survival (4), most patients ultimately succumb to their tumors. This is primarily due to the presence of a highly selective and regulated endothelium between blood and brain parenchyma known as the blood–brain barrier (BBB) (5), which limits the entry of therapeutics into the brain tissue where tumors are located. The BBB, characterized by a unique cellular architecture of endothelial cells (ECs), pericytes (PCs), and astrocytes (ACs) (6, 7), displays up-regulated expression of junctional proteins and reduced paracellular and transcellular transports compared to other endothelia (8). While this barrier protects the brain from toxins and pathogens, it also severely restricts the transport of many therapeutics, as evidenced by the low cerebrospinal fluid (CSF)-to-plasma ratio of most chemotherapeutic agents (9). There is thus an important need to develop new delivery strategies to cross the BBB and target tumors, enabling sufficient drug exposure (10).

Despite rigorous research efforts to develop effective therapies for high-grade gliomas, the majority of trialed therapeutics have failed to improve outcomes in the clinic, even though the agents in question are effective against tumor cells in preclinical models (11). This highlights the inability of current preclinical models to accurately predict the performance of therapeutics in human patients. To address these limitations, we developed an *in vitro* microfluidic model of vascularized GBM tumors embedded in a realistic human BBB vasculature. This BBB-GBM platform features brain microvascular networks (MVNs) in close contact with a GBM spheroid, recapitulating the infiltrative properties of gliomas observed in the clinic (12) and those of the brain tumor vasculature, with low permeability, small vessel diameter, and increased expression of relevant junctional and receptor proteins (7). This platform is well suited for quantifying vascular permeability of

Significance

The blood–brain barrier represents a major therapeutic challenge for the treatment of glioblastoma, and there is an unmet need for *in vitro* models that recapitulate human biology and are predictive of *in vivo* response. Here, we present a microfluidic model of vascularized glioblastoma featuring a tumor spheroid in direct contact with self-assembled vascular networks comprising human endothelial cells, astrocytes, and pericytes. This model was designed to accelerate the development of targeted nanotherapeutics and enabled rigorous assessment of a panel of surface-functionalized nanoparticles designed to exploit a receptor overexpressed in tumor-associated vasculature. Trafficking and efficacy data in the *in vitro* model compared favorably to parallel *in vivo* data, highlighting the utility of the vascularized glioblastoma model for therapeutic development.

Competing interest statement: R.D.K. is a co-founder of AIM Biotech that markets microfluidic systems for three-dimensional culture and receives research funding from Amgen and Biogen. P.T.H. is a co-founder and member of the board of LayerBio, a member of the Board of Alector, a member of the Scientific Advisory Board of Moderna, and receives research funding from Shepherd Pharmaceuticals, Novartis, and SecuraBio. All other authors report no competing interests.

Copyright © 2022 the Author(s). Published by PNAS. This open access article is distributed under Creative Commons Attribution-NonCommercial-NoDerivatives License 4.0 (CC BY-NC-ND).

¹J.P.S. and C.H. contributed equally to this work.

²Present address: Department of Oncologic Pathology, Dana-Farber Cancer Institute, Boston, MA 02115.

³R.D.K. and P.T.H. contributed equally to this work.

⁴To whom correspondence may be addressed. Email: rdkamm@mit.edu or hammond@mit.edu.

This article contains supporting information online at <http://www.pnas.org/lookup/suppl/doi:10.1073/pnas.2118697119/-/DCSupplemental>.

Published June 1, 2022.

therapeutics and simultaneously investigating modes of transport across the BBB and into GBM tumor cells.

There is strong rationale for developing therapeutic nanoparticles (NPs) for GBM and other brain tumors, as they can be used to deliver a diverse range of therapeutic agents and, with appropriate functionalization, can be designed to exploit active transport mechanisms across the BBB (13, 14). Liposomal NPs have been employed in the oncology clinic to improve drug half-life and decrease systemic toxicity (15), but, to date, no nanomedicines have been approved for therapeutic indications in brain tumors. We hypothesize that a realistic BBB-GBM model composed entirely of human cells can accelerate preclinical development of therapeutic NPs. Using our BBB-GBM model, we investigated the trafficking of layer-by-layer NPs (LbL-NPs) and ultimately designed a GBM-targeted NP. The LbL approach leverages electrostatic assembly to generate modular NP libraries with highly controlled architecture. We have used LbL-NPs to deliver a range of therapeutic cargos in preclinical tumor models (16, 17) and have recently demonstrated that liposomes functionalized with BBB-penetrating ligands improved drug delivery across the BBB to GBM tumors (18). Consistent with clinical data (19), we observed that the low-density lipoprotein receptor-related protein 1 (LRP1) was up-regulated in the vasculature near GBM spheroids in the BBB-GBM model and leveraged this information to design and iteratively test a library of NPs. We show that the incorporation of angiopep-2 (AP2) peptide moieties on the surface of LbL-NPs leads to increased BBB permeability near GBM tumors through LRP1-mediated transcytosis. With intravital imaging, we compared the vascular permeabilities of dextran and LbL-NPs in the BBB-GBM platform to those in mouse brain capillaries and validated the predictive potential of our *in vitro* model. Finally, we show the capability of the BBB-GBM platform to screen therapeutic NPs and predict *in vivo* efficacy, demonstrating improved efficacy of cisplatin (CDDP) when encapsulated in GBM-targeting LbL-NPs both *in vitro* and *in vivo*.

Results

A Vascularized Glioblastoma Model for the Quantification of Vascular Permeability. To recapitulate the GBM microenvironment and evaluate the transport of therapeutics across the BBB, we developed an *in vitro* BBB-GBM model in a microfluidic device. This platform features a tumor spheroid (GBM spheroid) composed of cells from a patient-derived xenograft (PDX) glioblastoma cell line cocultured with PCs, which is embedded in a BBB vascular system in which induced pluripotent stem cell-derived ECs (iPS-ECs), PCs, and ACs self-assemble into perfusable vascular networks (20, 21) (Fig. 1*A*). We chose to use the GBM22 cell line from the Mayo Clinic Brain Tumor PDX National Resource (22, 23) for these initial studies because it is well-characterized and has been used extensively in preclinical studies as an orthotopic xenograft (24, 25). GBM22 is a PDX line derived from a tumor fitting the World Health Organization 2016 classification of glioblastoma, isocitrate dehydrogenase-wild type, with O6-methylguanine-DNA-methyltransferase promoter methylation. The patient was treatment-naïve at the time the cell line was generated, though murine models showed a survival benefit with standard therapies, such as radiation and temozolomide (23). GBM spheroids were generated by combining GBM22 cells with brain PCs in a 4:5 ratio, recapitulating tumor–stromal ratios found *in vivo* and ensuring that tumors remain compact throughout the

culture and prior to injection in the devices with the cells of the BBB (26). GBM spheroids grew in close contact with their surrounding vasculature, resulting in a vascularized GBM model after 7 d of culture. The spheroids grew rapidly in the microfluidic devices and appeared to co-opt the surrounding BBB vasculature, similar to what is observed in high-grade glioma patients and in animal models of GBM (27, 28) (*SI Appendix*, Fig. S1). Comparable vessel-density measurements were observed in both proximal and distal regions to the GBM spheroid (29) (*SI Appendix*, Fig. S1).

Despite a commonly held belief that the BBB is disrupted in human glioblastoma, analyses from patient samples have shown that vessels near high-grade gliomas often exhibit the same integrity and density as vessels found in the healthy brain tissue, depending on their level of infiltration and location within the tumor (30, 31). Particularly, it has been shown that for developing or residual glioma tumors with smaller sizes, the BBB remains intact, and the tumor mass is sustained by normal brain vessels (32). To evaluate our platform in this context, we assessed paracellular permeability to dextran by measuring changes in intensity following fluorescent dextran injection in the vasculature via confocal microscopy (21). Three regions of interest (ROIs) were compared: 1) vessels in devices without GBM tumor (no GBM spheroid), 2) vessels far away (>2,500 μm) from the GBM tumor (far from GBM), and 3) vessels in close proximity to the GBM tumor where co-option is observed (near GBM) (Fig. 1*B*). We measured no differences in vascular permeability in these three regions, suggesting that tight junctions remain intact, even in locations where GBM co-option is evident (Fig. 1*C*). These findings are striking in comparison with analogous measurements performed by our group using vascularized ovarian or lung tumor models, where vessel permeability was found to be threefold larger near the tumor (29). The undisturbed BBB near GBM tumors in this platform attests to the ability of GBM cells to invade and co-opt the vasculature without modifying its properties. This is also demonstrated by unaltered tight and adherens junction protein expressions at endothelial borders in regions of vascular co-option when compared to healthy BBB vessels without GBM tumors (*SI Appendix*, Fig. S1). These results indicate that our BBB-GBM platform is realistic in modeling glioblastoma vasculature, particularly in early tumor development or in recurrent tumor progression following resection, where developing tumors are sustained by normal BBB vessels.

The unaltered paracellular permeability of BBB vessels near developing GBM tumors suggests that enhanced localized transport across the BBB via disrupted endothelial junctions is unlikely. Delivery of therapeutics through ligand-based transcellular transport thus offers an avenue for targeted trafficking of therapeutics near GBMs. LRP1, a transport receptor involved in various cellular processes at the BBB, including lipid and lipoprotein metabolism and protease degradation (33), has been shown to be up-regulated in GBMs and their surrounding vasculature (34). As a result, there is interest in the design of therapeutics employing LRP1-mediated transport to cross the BBB and specifically target GBM (35–37). We investigated LRP1 expression in the BBB-GBM model and found that the presence of GBM spheroids increases LRP1 expression in vessels both near and far from the spheroid, compared to control devices without tumor (Fig. 1*D* and *E* and *SI Appendix*, Fig. S1). LRP1 expression was also evidenced within GBM tumor cells. These results guide our subsequent NP design for enhanced targeted delivery across the BBB near GBM tumors.

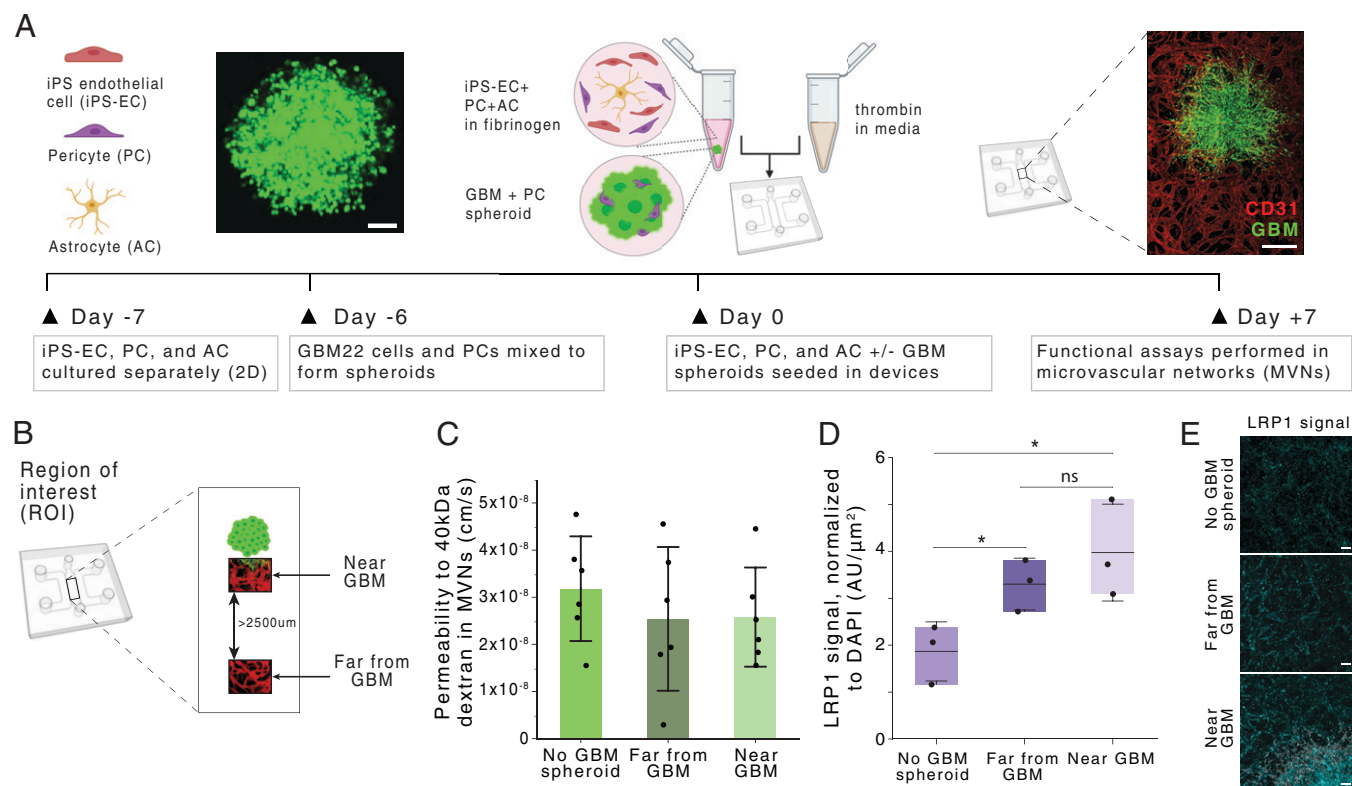


Fig. 1. Generation and characterization of a glioblastoma BBB MVN model (BBB-GBM model). (A) Schematic of BBB-GBM formation in a microfluidic device. (Scale bars: 100 μm [Left] and 500 μm [Right].) (B) ROIs identified spatially within the BBB-GBM model, with far from GBM ROIs identified to be at least 2,500 μm away from the GBM spheroid. (C) Permeability to 40-kDa dextran in the vascular networks across different ROI locations; each point represents $n = 1$ device. (D) Expression of LRP1 across different ROI locations, as assessed via immunofluorescence staining; each point represents $n = 1$ device. (E) Representative micrographs of LRP1 staining quantified in D. (Scale bars: 100 μm .) In all graphs, bars represent mean \pm SD. ns, not significant. * $P < 0.05$. Statistical analyses are described in *Materials and Methods*. AU, arbitrary units; 2D, two-dimensional.

Targeted NPs Cross BBB Vessels Near GBM Tumors via LRP1-Mediated Transport. We next employed the LbL method to develop an NP with enhanced trafficking to GBM cells through tumor-associated vasculature. LbL-NPs consist of a charged NP core and polyelectrolyte multilayer shell; for this study, we started with a liposomal NP core and layered with poly-(L-arginine) and propargyl-modified poly-(L-aspartic acid) (pPLD) as described to generate a click-compatible LbL-NP (38). We chose to use a propargyl modification extent of 12% in order to preserve the inherent “stealth” benefits from the anionic, hydrated PLD coating (39), while also incorporating sufficient amounts of targeting ligand. The surface of the NP was functionalized with AP2, a peptide designed to target the BBB via interaction with the LRP1 receptor overexpressed in GBM vessels (40) (Fig. 1 D and E), generating NPs with favorable size and surface potential for drug-delivery applications (*SI Appendix, Table S1*).

We first investigated the NP-cell association of fluorescently labeled (Cyanine5) bare (Bare NPs) and LbL NPs with an outer surface of pPLD (pPLD NPs) or pPLD functionalized with AP2 (AP2 NPs) (Fig. 2A) with the four cell types in the BBB-GBM model (iPS-ECs, PCs, ACs, and GBM22) using flow cytometry. AP2 NPs exhibited the highest NP-associated fluorescence in all cell lines compared to bare or pPLD NPs, and NP internalization in GBM cells was confirmed by microscopy (*SI Appendix, Fig. S2*). The AP2 NP trend was amplified in iPS-ECs, which have high native LRP1 expression and are the first cell type encountered by NPs when crossing the BBB model. We next investigated the ability of NPs to associate with GBM spheroids in the absence of vascular networks to

ensure that NPs can deliver encapsulated cargo to the cell of interest. Incubation with the different NP formulations showed increased accumulation of AP2 NPs in GBM spheroids compared to bare NPs (Fig. 2 B and C).

NP trafficking was assessed by quantifying vascular permeability, as previously done for various therapeutic molecules (41, 42) (Fig. 1C). Of the three NP formulations, AP2 NPs exhibited a significant increase in permeability near the GBM tumor compared to BBB vessels without tumors (Fig. 2 D and E and *SI Appendix, Fig. S3*). This trend was not only observed with liposomal NPs, but also held true with polystyrene NP cores (*SI Appendix, Fig. S3*), indicating that these effects are most likely stemming from the LbL surface functionalization with AP2. In control BBB microvessels (without tumors), bare NPs had slightly higher permeability than pPLD or AP2 NPs (*SI Appendix, Fig. S3*), which we hypothesize to result from two factors. First, the addition of peptides in place of charged groups on the surface may hinder nonspecific transport in a setting with low expression of the targeted receptor. In addition, we identified a size threshold for NP transport across the in vitro BBB, and layered functionalized NPs are slightly larger than bare liposome NPs (z-average diameter of 106.2 nm for bare NPs, 164.8 nm for pPLD NPs, and 163.5 nm for AP2 NPs; *SI Appendix, Table S1*). To further investigate this size threshold, we chose to use commercially available carboxylated polystyrene NP cores because they are highly uniform in size and amenable to LbL assembly. Testing a range of sizes revealed that nonfunctionalized NPs ≥ 100 nm in diameter cannot cross the in vitro BBB (*SI Appendix, Fig. S3*). However, the same 100-nm-diameter polystyrene NPs with negligible permeability

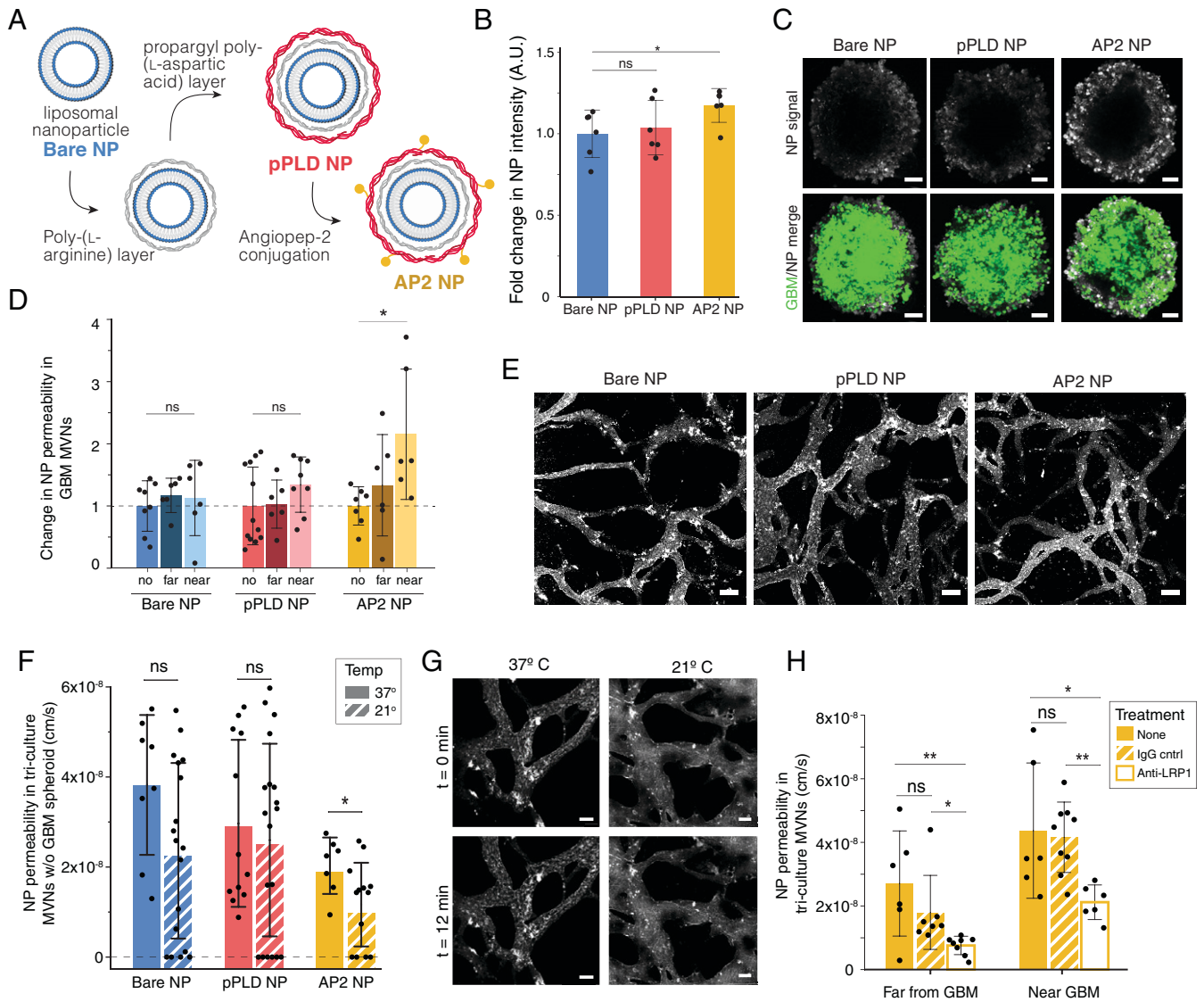


Fig. 2. Functionalized LbL-NPs cross BBB MVNs near GBM spheroids via LRP1-mediated transport. (A) LbL assembly of AP2 NPs. (B) Fold change in mean fluorescence intensity (MFI) of NPs in GBM spheroids without vascular networks, normalized to bare NP; points represents $n = 1$ spheroid. (C) Representative GBM spheroids after 12-min NP incubation, as quantified in B. (Scale bars: 100 μm .) (D) NP permeability in networks with no GBM spheroid (no) and in regions near and far from a GBM spheroid, normalized to the no spheroid device; points represent $n = 1$ ROI; $n = 6$ devices per condition were considered. (E) Representative images of NPs in the BBB microvessels at $t = 0$ min following NP perfusion; time-lapse images over 12 min were used to determine permeabilities in D. (Scale bars: 100 μm .) (F) BBB vessel permeabilities to the three NP formulations in networks without GBM spheroids at 37°C and 21°C. Points represent $n = 1$ ROI; $n = 4$ devices per condition were considered. (G) Representative images of AP2 NPs at $t = 0$ and $t = 12$ min, as quantified in F. (Scale bars: 50 μm .) (H) BBB vessel permeabilities to AP2 NPs at 37°C following incubation for 30 min with anti-LRP1 or IgG control antibodies. Points represent $n = 1$ ROI; for antibody conditions, $n = 4$ devices were considered; $n = 6$ nontreated devices. Throughout, bars represent mean \pm SD. ns, not significant. * $P < 0.05$; ** $P < 0.01$. Statistical analyses are described in *Materials and Methods*. A.U., arbitrary units; w/o, without.

showed a significant increase in permeability near the GBM tumor after LbL surface functionalization with AP2 (*SI Appendix, Fig. S3*). Although polystyrene and liposomal NPs of comparable sizes exhibit similar permeability changes following LbL surface functionalization with AP2, the two NP cores have vastly different physiochemical properties and cross the *in vitro* BBB at different orders of magnitude (permeability of polystyrene NPs $\sim 10^{-9}$ cm/s compared to $\sim 10^{-8}$ cm/s for liposomal NPs). This finding is consistent with literature associating the high stiffness of polystyrene NPs [Young's modulus on the order of $\sim 10^9$ Pa versus $\sim 10^6$ Pa for liposomes (43, 44)] with decreased cell internalization due to less efficient internalization mechanisms for stiffer nanomaterials (45–47). In addition, liposomal NP cores are more translationally relevant, as they can be used to encapsulate a range of therapeutics for the treatment of GBM tumors.

Having demonstrated increased LRP1 expression in tumor-associated vasculature and increased AP2 NP permeability near GBM spheroids, we hypothesized that AP2 NPs cross the BBB via transcytosis (48) and, more specifically, via LRP1-mediated transport. An active mode of transport was validated in the *in vitro* BBB vessels by reducing temperatures from 37°C to 21°C to prevent vesicle detachment from the cell membrane and transitioning across the cytoplasm to transport NPs from the luminal to the abluminal side of the vessels (42). Indeed, permeability of AP2 NPs was reduced at 21°C, in line with our hypothesis that AP2 NPs cross the BBB via receptor-mediated transcytosis (Fig. 2 F and G). As expected, *in vitro* BBB permeability to 40-kDa dextran, which is expected to cross the endothelium via paracellular transport, was not affected by temperature changes (*SI Appendix, Fig. S3*), confirming that reduced temperatures do not affect the functional

properties of the endothelium and its paracellular permeability. The bare and pPLD NP formulations also exhibited small, yet not significant, decreases in permeability, suggesting that NPs of this size, regardless of their functionalization, cross the BBB at least in part via vesicular transport (49, 50). These observations are intriguing and consistent with recently reported findings that the majority of NP transport across the tumor-associated endothelium occurs via active processes (51). Permeability of AP2 NPs was decreased following LRP1 neutralization compared to IgG control in regions near and far from the GBM spheroid, validating AP2 NP shuttling via the LRP1 receptor in the BBB-GBM model (Fig. 2H). In addition to treatment with antibodies affecting transport across the BBB, we also show the potential for testing neutralizing antibodies that directly affect GBM tumor growth (SI Appendix, Fig. S4). Following daily administration of anti-vascular endothelial growth factor (anti-VEGF), tumor size was measured over time, and the GBM spheroid area was found to increase in the presence of a therapeutic anti-VEGF antibody, a somewhat paradoxical finding, though it has been observed in clinical series of patients with recurrent GBMs treated with bevacizumab (52). These results highlight the testing capabilities of the BBB-GBM model, where NP formulations and antibodies can be assayed with high spatiotemporal resolution, to identify their transport properties into tumors.

The In Vitro BBB Model Accurately Predicts In Vivo Permeability.

To evaluate the ability of the BBB-GBM platform to mimic the more complex in vivo environment, we quantified permeability of dextran and functionalized NPs in mouse capillaries via intravital imaging. Following NP and dextran intravenous administration in animals, time-lapse images were acquired through a cranial window to quantify vascular permeability, as performed in the in vitro devices (Fig. 3A, SI Appendix, Fig. S5, and Movie S1). Both dextran and NP signals were clearly observed in mouse cortical capillaries with comparable sizes to in vitro BBB vessels (Fig. 3B and SI Appendix, Fig. S4 and Table S2). Dextran permeability values obtained with the imaging and analysis techniques described here were ~one order of magnitude smaller than measurements performed by other groups in mouse or rat brain capillaries (53, 54) (SI Appendix, Table S3). Remarkably, values obtained in mouse BBB vessels were highly consistent with those obtained in the BBB microvascular device for both 10- and 40-kDa dextran (Fig. 3C and SI Appendix, Fig. S5). Similarly, NP permeabilities corresponded closely to values from the in vitro BBB model without tumors (Fig. 3D). In addition to having comparable morphological properties (SI Appendix, Table S2), the consistent permeability measurements in vitro and in vivo highlight the ability of the in vitro BBB model to recapitulate functional aspects of the in vivo BBB. Of note, permeability studies in mouse BBB capillaries (without tumors) were performed at depths less than 150 μm below the dura, where imaging resolution is optimal. Performing comparable measurements in vessels near GBM tumors in vivo would require superficial tumor implantation, which is technically challenging and less clinically relevant than an orthotopic model in the deeper regions of the brain, as tumors are likely to extravasate and establish outside the confines of the BBB (55).

Therapeutic NPs Effectively Target Tumors in the BBB-GBM Model and In Vivo. In addition to studying transport, the BBB-GBM model offers the rare opportunity to assess therapeutic efficacy of new agents in the highly relevant setting of microscopic tumor burden. The extent of surgical resection is an

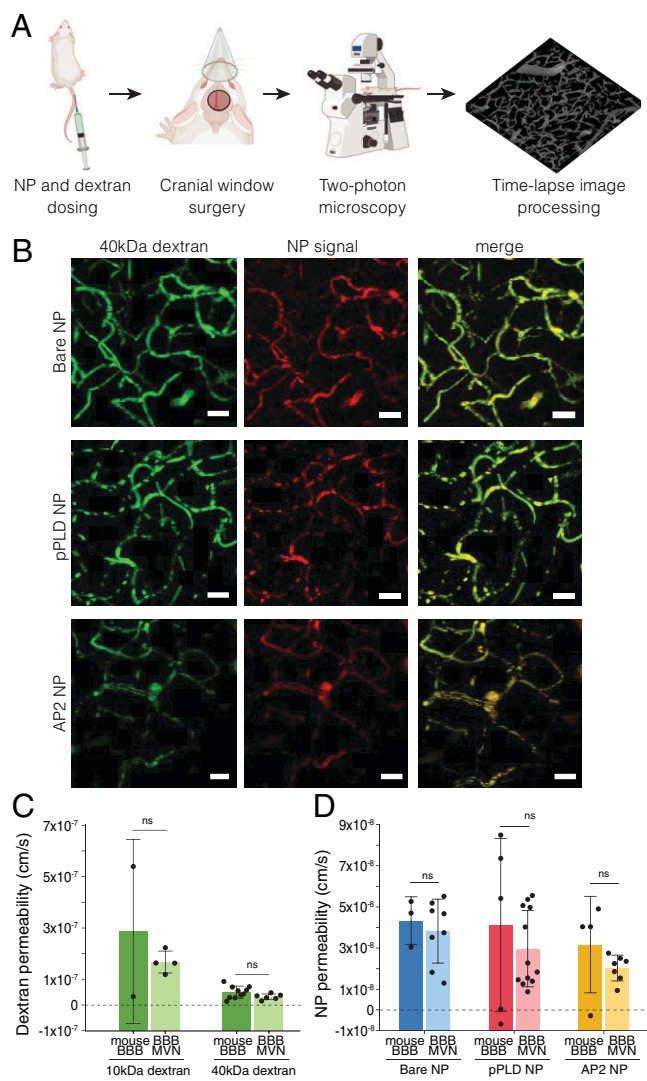


Fig. 3. In vivo BBB permeability assessed by intravital microscopy is consistent with the in vitro BBB model. (A) Workflow of intravital imaging, in which fluorescent NPs and dextran are dosed systemically, and time-lapse imaging is performed in intact brain capillaries. (B) Representative images of 40-kDa dextran and NP formulations perfused in mouse BBB capillaries. (Scale bars, 20 μm .) (C) BBB permeabilities to fluorescently labeled dextran (10 and 40 kDa) in mouse BBB capillaries and in vitro BBB microvessels (no tumors). Points represent $n = 1$ device; $n = 2$ mice were considered for 10-kDa dextran and $n = 10$ mice for 40-kDa dextran. (D) BBB permeabilities to the three NP formulations in mouse BBB capillaries and in vitro BBB microvessels (no tumors). Points represent $n = 1$ ROI; $n = 6$ independent devices per condition were considered; $n = 3$ to 5 mice were considered per condition. Bars represent mean \pm SD. ns, not significant. Statistical analyses are described in *Materials and Methods*.

important prognostic factor in that achieving a gross total resection portends improved survival for GBM patients, but most tumors recur due to microscopic tumor deposits near the resection cavity (56, 57). To assess the therapeutic potential of LbL-NPs for GBM and the preclinical value of the BBB-GBM model, we next encapsulated the DNA-damaging agent CDDP in the liposome core of the NPs (SI Appendix, Fig. S6). We hypothesized that a selective mode of delivery of CDDP to GBM tumors would lead to improved efficacy and reduced toxicity in the healthy surrounding brain tissue and blood vessels. CDDP was chosen in this study for its nonspecific mechanism of action and its poor BBB penetration [<0.04 CSF-blood ratio (9)] to evaluate the influence of drug delivery. The BBB-GBM model was instilled with 6 μM free CDDP, CDDP

loaded into bare NPs (bare CDDP NPs, formulated at 7.9 weight% with respect to lipid), or CDDP loaded into AP2 NPs (AP2 CDDP NPs, 4.6 weight%; *SI Appendix, Table S1*). CDDP dosing was based on previously determined *in vitro* IC₅₀ values for GBM22 cells (*SI Appendix, Fig. S6*) and was continued daily for 4 d via perfusion in BBB microvessels. At the end of the dosing period, all spheroids treated with CDDP containing formulations decreased in size significantly compared to the untreated control, with differences evident as early as 24 h following initial treatment (Fig. 4 *A* and *B*).

We next assessed trafficking of CDDP-loaded NPs across the BBB and into the tumor space by quantifying NP association with the GBM spheroid over the course of treatment. Bare CDDP NPs initially exhibited higher association with GBM tumors compared to AP2 CDDP NPs; however, this trend was reversed by day 4 of treatment (Fig. 4*C*); we hypothesize that specific interactions between LRP1 and AP2 CDDP NPs

lead to higher NP accumulation in the spheroid over time. Although all CDDP formulations resulted in tumor growth inhibition, we hypothesized that improved accumulation of AP2 CDDP NPs in GBM cells with repeated dosing may enhance the therapeutic index of the drug and result in reduced cytotoxicity in the local BBB vessels. This was evaluated by using the Sytox nucleic acid stain to label dead cells in three ROIs (far, near, and inside GBM spheroids), following treatment with free CDDP, bare CDDP NPs, or AP2 CDDP NPs. Treatment with AP2 CDDP NPs resulted in the largest increase in Sytox signal inside GBM tumors relative to untreated devices (Fig. 4 *D* and *E*). Near and far from GBM tumors, Sytox signal was minimally increased with all CDDP formulations compared to untreated devices, except for free CDDP, which resulted in significant increases in Sytox. Following treatment with the CDDP formulations, regions of the BBB-GBM devices were extracted for qRT-PCR. Annexin V,

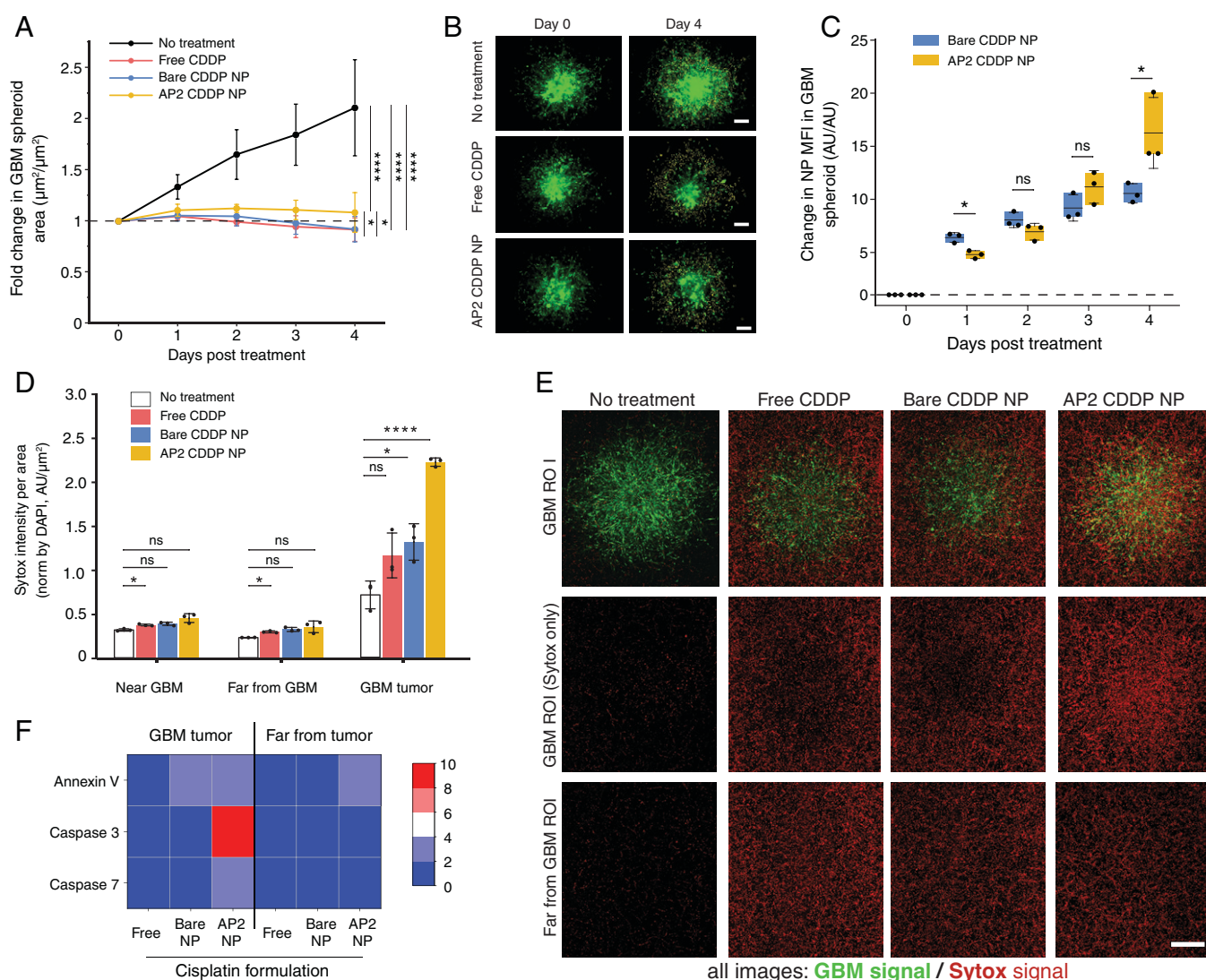


Fig. 4. Encapsulation in LBL-NPs improves efficacy and targeted delivery of CDDP in BBB-GBM. (A) GBM spheroid size in BBB-GBM model following treatment with free CDDP, CDDP encapsulated in bare NPs (Bare CDDP NP), or CDDP encapsulated in AP2 NPs (AP2 CDDP NP), compared to untreated devices. Points represent mean \pm SD of $n = 6$ devices. (B) Representative fluorescent micrographs quantified in A. (Scale bars: 200 μm .) (C) Change in MFI of NP signal in GBM tumors in the BBB-GBM device over time, following treatment with fluorescently tagged bare- or AP2-CDDP NPs. Points represent $n = 1$ device. (D) MFI of Sytox signal per area (normalized by DAPI, AU/ μm^2) in the three ROI locations considered in BBB-GBM devices after treatment with free CDDP, bare CDDP NPs, or AP2 CDDP NPs and compared to control devices without treatment. Points represent $n = 1$ device. (E) Representative fluorescent micrographs quantified in D. (Scale bar: 500 μm .) (F) Heatmap of cell death gene-expression levels in two ROIs of the devices (inside the GBM tumor and far from the tumor), as quantified by qRT-PCR. Bars represent mean \pm SD. ns, not significant. * $P < 0.05$; **** $P < 0.0001$. Statistical analyses are described in *Materials and Methods*. AU, arbitrary units.

Caspase 3, and Caspase 7 transcripts were all elevated in GBM tumors collected from devices treated with AP2 CDDP NPs compared to the other CDDP formulations (Fig. 4*F*). There were no major differences in the expression of genes involved in apoptosis far from the tumor for the different CDDP formulations. Taken together, we performed four quantitative assays from each device in series: spheroid growth over time (Fig. 4*A* and *B*), NP colocalization (Fig. 4*C*), cell viability (Fig. 4*D* and *E*), and gene expression (Fig. 4*F*). With these, we show that treatment with CDDP decreases the morphologic size of GBM spheroids regardless of formulation, but encapsulating CDDP within LbL-NPs with AP2 surface functionalization results in more effective cell killing, with higher cell death in GBM spheroids and minimal damage to the healthy surrounding BBB vasculature. This is further supported by focally increased expression of genes involved in apoptosis in tumors treated with AP2 CDDP NPs, consistent with a pharmacodynamic effect from CDDP.

To test the ability of the BBB-GBM device to predict in vivo response, we employed the same CDDP NP formulations in an orthotopic xenograft model generated using the same patient-derived GBM cells used in the BBB-GBM device. To mirror the time frame of the in vitro studies, we quantified tumor volume before and after a short dosing period using MRI (Fig. 5*A*). CDDP formulations were dosed via tail vein every 3 d at a dose of 0.75 mg/kg CDDP. This dose was chosen as the highest attainable dose based on limits of passive encapsulation and injection volume and, accounting for conversion from mouse to human (58), is notably lower than the dose employed in GBM clinical trials (59) (2.3 mg/m²/dose compared to 30 mg/m²/dose in clinical trials). Despite this limitation, we observed a slower growth trajectory in tumors of animals treated with AP2 CDDP NPs compared to those of animals treated with equivalent CDDP doses in free form ($P = 0.047$) (Fig. 5*B* and *SI Appendix, Fig. S7*), consistent with the improved accumulation of AP2 CDDP NPs in tumors in vitro. Levels of cleaved caspase-3 (CC-3) were also increased in tumor tissue after treatment with AP2 CDDP NPs compared to empty liposome control ($P = 0.0019$) (Fig. 5*C* and *D*), consistent with increased DNA damage identified in the in vitro BBB-GBM device.

Taken together, we show that encapsulation of CDDP in an LbL-NP with AP2 surface functionalization leads to improved efficacy in vitro using a BBB-GBM device and in vivo using an analogous orthotopic xenograft model. These findings highlight the impact of LbL surface functionalization in nanomedicine and contribute to the existing body of literature supporting AP2 as a promising targeting BBB moiety. Importantly, the in vitro human BBB-GBM model allowed us to rigorously interrogate the trafficking and therapeutic effects of multiple NP formulations in a realistic setting predictive of in vivo effects. The high spatiotemporal resolution of our in vitro BBB-GBM model and its use in dissecting and investigating modes of transport at the BBB make it a valuable preclinical testing platform to speed the development of brain tumor-directed therapies.

Discussion

In this study, we present an in vitro model of the GBM tumor microenvironment that features perfusable human BBB microvessels coming in direct contact with tumor cells. This innovative design provides a robust platform to study the trafficking of tumor-directed therapies across the BBB. With recent

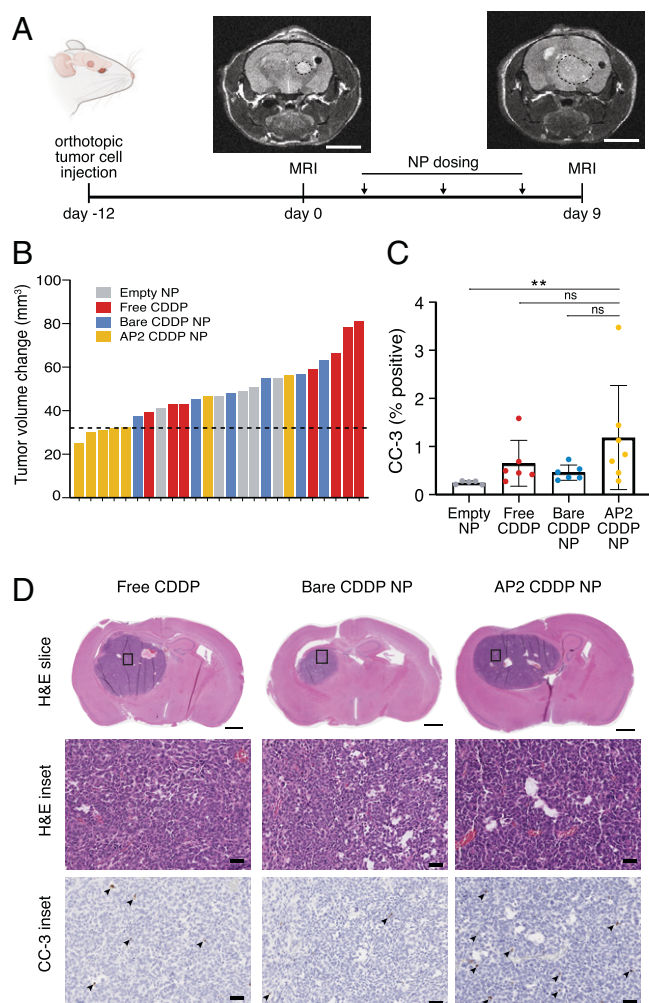


Fig. 5. BBB-GBM device predicts differential effects of CDDP NP formulations in an orthotopic in vivo model. (A) Timeline of in vivo study with orthotopic GBM tumors using MRI to monitor response to therapeutic NPs. (Scale bars, 4 mm.) (B) Waterfall plot for change in tumor volume after treatment on the y axis, where each bar represents one mouse; dotted line is the median tumor volume change for the AP2 NP group. (C) Quantification of CC-3 staining in tumor tissue. Each dot represents $n = 1$ mouse. (D) Representative immunohistochemistry micrographs with hematoxylin and eosin (H&E) staining (for context) and CC3, as quantified in C; arrowheads denote CC-3-positive cells. (Scale bars: 50 μ m [Middle and Bottom] and 1 mm [Top].) Bars represent mean \pm SD. ns, not significant. $***P < 0.01$. Statistical analyses are described in *Materials and Methods*.

advances in in vitro technologies and a push for personalized patient models, there has been increased interest in the design of three-dimensional, preclinical human GBM assays (60–62). While existing three-dimensional platforms can recapitulate some features of the GBM microenvironment, such as cell–cell and cell–matrix contacts, most lack stromal cells such as ECs, ACs, PCs, and immune cells, all of which are known to have key functions in promoting tumor growth (63). For drug-delivery applications, and in particular when considering NP transit, perfusable vasculature is a key component to consider. Coculture models, including GBM cells and ECs, are very useful for studies of the tumor microenvironment, but often lack perfusable vasculature (64, 65) or feature tube-like vessels of large diameters that do not come in direct contact with GBM cells (66, 67). Recently, organoid cultures of patient-derived glioma stem cells have been employed to better recapitulate GBM–vascular interactions; however, the self-assembled vessels in these cultures are typically not perfusable, which limits their

use in the context of drug delivery across the BBB and into tumors (68). Here, we address these limitations by incorporating a GBM tumor spheroid into perfusable self-assembled vascular networks composed of iPSECs, PCs, and ACs. We have previously demonstrated that these vasculatures recapitulate several properties of the human BBB, including relevant morphology and cellular architecture, low values of permeability, and expression of junction and transport proteins (20, 21, 69). In the BBB-GBM model, spheroids proliferate and infiltrate the surrounding vasculature, resulting in a physiologically relevant model of vascularized GBM tumors co-opting their adjacent vessels, as observed in patient brain tumors (27, 70). The morphology, cellular organization, and barrier function of the BBB are recapitulated in our model, which features the smallest diameters of perfusable BBB vessels reported to date (21, 71). Some limitations of our model include the lack of relevant fluid flows, which can be addressed with the use of a pressure controller, as previously done (72, 73), and the lack of immune cells or neurons of the brain, which are involved in transport and clearance of solutes at the BBB (74). These will be a focus of future work.

Our system has a number of potential applications for the study of the BBB-GBM interface, ranging from fundamental biology to experimental therapeutics. Here, we report one compelling application: the design, optimization, and evaluation of a targeted therapeutic NP. Leveraging increased expression of LRP1 on blood vessels in proximity to GBM spheroids, we synthesized LbL-NPs with AP2 on the surface and investigated their trafficking across the BBB and into GBM spheroids. Compared to conventional NP design and optimization, which generally involves two-dimensional assays in one or a few immortalized cell lines (75), we were able to evaluate NP trafficking rapidly and quantitatively in a three-dimensional environment that accurately recapitulates human GBM. We also probed the mechanisms of functionalized NP trafficking with high spatiotemporal resolution and confirmed that our AP2 NPs cross the vasculature via an active process mediated by the LRP1 receptor. These data are consistent with receptor-mediated transcytosis as the means by which AP2 NPs cross the BBB.

To evaluate the clinical translatability of our *in vitro* model, we performed analogous permeability assays in the murine brain using *in vivo* imaging and confirmed that our model accurately recapitulates the *in vivo* setting. To our knowledge, direct comparisons of *in vitro* and *in vivo* BBB permeabilities using the same measurement technique have not been reported. More importantly, the majority of animal permeability measurements are performed at low resolution, utilizing two-dimensional measures and small ROIs (53, 54, 76), which can impact the resulting permeability measurements (42). Our approach circumvented these challenges using three-dimensional volumes containing several interconnected BBB capillaries, resulting in permeability values that matched those of the *in vitro* model with great accuracy. We have previously identified that species differences can play a role in differences in protein transcytosis (41). The protein mediating transcytosis in our study, LRP1, has been well characterized and shown to be conserved between mouse and human with consistent expression in brain microvessels in both species (77), but it is important to consider species-related differences when comparing *in vitro* and *in vivo* models, and we plan to explore this further in future work. Another difference between our *in vitro* and *in vivo* models is a lack of continuous flow *in vitro*. This is a limitation of the current study, but it can be addressed in the future by employing a newly designed pumping system that is

capable of providing long-term perfusion with microfluidic platforms of the type used in the present study (72). Altogether, these findings support the continued development of *in vitro* BBB models for translational applications.

In addition to its ability to predict permeability *in vivo*, another important feature of our BBB-GBM platform is its ability to model clinical scenarios with significant treatment challenges, such as residual microscopic tumor deposits after surgery. Even after a gross total resection, highly proliferative and invasive residual tumor cells are often found beyond the margins of resected gliomas, leading to tumor recurrence (78). Given the dismal prognosis of recurrent GBM, developing effective treatments for recurrent tumors is of the utmost importance. Our BBB-GBM model, with its barrier properties mimicking the human BBB, provides a realistic tool to design and evaluate alternative therapeutics targeting residual or recurrent tumors, surrounded by an intact BBB. One of the key advantages of our model is the ability to assess changes in BBB microvasculature—both biologic and functional—in the presence of a PDX tumor spheroid, paving the way for a wide range of basic and translational investigations in future work.

We utilized the BBB-GBM model to develop a panel of LbL-NPs and test their trafficking and therapeutic effects, along with untargeted liposomes and polymeric NPs. By functionalizing the surface of CDDP NPs with AP2, we showed improved NP accumulation and increased apoptosis in the GBM spheroid with minimal damage to surrounding healthy blood vessels, highlighting the potential for rationally designed nanotherapeutics to exert a selective therapeutic effect based on differential trafficking in tumor-associated vasculature. We complemented these studies with analogous investigations in an orthoptic intracranial murine tumor model to determine whether these results correlate with NP efficacy on a larger scale and observed slower tumor growth in mice treated with AP2 CDDP NPs, despite subclinical dosing. However, we hypothesize that the rapid growth and large tumor size at the study endpoint mitigated our ability to detect differential therapeutic effects, which may be more evident in a microscopic tumor setting. This is a common limitation of *in vivo* GBM studies and is further motivation to develop a predictive *in vitro* model for testing of future, more potent therapies. With the *in vitro* model, we were able to get around this limitation to generate a vascularized model of recurrent GBM tumor in the early stages of development, where GBM tumors do not significantly encroach on the surrounding vasculature. The *in vitro* model enables the detection of biological changes at the BBB before the GBM tumor is large enough to mechanically disrupt the BBB, thus allowing for the identification of therapeutic avenues for drug delivery (in our case, AP2 NPs through LRP1-mediated transport) prior to BBB damage.

With increasing interest in the development of personalized medicine platforms for the testing of therapies, we anticipate that our BBB-GBM model may be able to address this need in the future if paired with patient cells isolated at the time of surgery. This could address a limitation of our current model—the lack of microglia or resident immune cells. Microglia are known to play important roles in clearance and have been increasingly recognized as having a role in GBM cell state and response to therapy (79); the ability to incorporate patient-derived, tumor-associated microglia would enhance the fidelity of our model and will be a focus for future work. Such a model could enable rapid drug screening with both clinical and investigational therapies. The BBB-GBM model presented in this study allows for real-time quantitative measurements of NP trafficking in live cells. This can also be performed via liquid

sampling through one of the ports of the device, as previously done (42), enabling comparisons of our *in vitro* model to *in vivo* central nervous system sampling performed via cerebral microdialysis (80). Connecting our BBB-GBM model to other organ-on-a-chip systems (e.g., liver, kidney, or lung) would also enable studies of NP pharmacokinetics with particles circulating in different organ models in addition to the BBB (81–84). Liquid sampling can also be performed through one port of the microfluidic device, as we have previously shown (42), for pharmacokinetic studies; this parallels tumor interstitial fluid sampling done *in vivo* or in the clinic (80). Another application of our model may be to address tumor heterogeneity in a systematic manner. Whereas we employed our vascularized GBM model with one PDX tumor model and tested a panel of functionalized NPs, our platform could be similarly employed to compare biologic and functional differences in the vasculature of multiple glioma models.

Our BBB-GBM platform provides a highly relevant resource for the scientific community studying GBM and other challenging brain tumors, particularly in the context of drug delivery with targeted NPs. Ultimately, realistic *in vitro* vascularized GBM models can advance our understanding of tumor-blood-vessel biology and accelerate the development of brain-penetrant therapeutics.

Materials and Methods

Study Design. The main objective of this study was to develop a vascularized GBM model and employ it to investigate the trafficking of LbL NPs. All *in vitro* studies utilized at least four devices per group. We validated the results of this study using intravital microscopy in non-tumor-bearing mice ($n = 3$ to 5 per group) and in an orthotopic xenograft mouse model ($n = 5$ to 7 mice per group).

For all experiments, devices and animals were allocated randomly across different groups. For tumor-burden quantification by MRI, all image analyses were performed in a blinded fashion. All animal experiments in this study were approved by the Institutional Animal Care and Use Committee (IACUC) for the Massachusetts Institute of Technology and were performed in accordance with the approved guidelines for animal experimentation from the Committee on Animal Care.

Cell Culture and Treatments. Human iPSC-ECs (Fujifilm Cellular Dynamics, catalog no. 11713), human brain PCs, and ACs (ScienCell) were cultured as described (20, 69). The high-grade glioma PDX line glioblastoma 22 (GBM22) originated in the Sarkaria laboratory, Mayo Clinic, and cell-line identity was confirmed by short tandem repeat testing.

Tumor Spheroid Formation. GBM22 and brain PCs were cocultured in a low-adhesion, 96-well plate (PrimeSurface 96M plate, Sbio) at a ratio of 4:5 to recapitulate tumor-stromal-cell ratios commonly observed in solid tumors (26) and ensure that the spheroids remained compact in the low-adhesion plates. Spheroids formed over several days by self-aggregation and were cultured for 6 to 7 d prior to seeding in the microfluidic devices as described (20, 69).

Device Fabrication and MVN Formation. The three-dimensional microfluidic devices employed in this study were fabricated by using soft lithography as described (70, 85) with dimensions outlined in detail elsewhere (86). Briefly, a larger device with a width of 3 mm for the central gel channel and height of 500 μm was employed to ensure that spheroids can occupy the center of the channel with sufficient space for the formation of surrounding MVNs. To recapitulate the *in vivo* organization of glioma tumors surrounded by brain capillaries, spheroids were carefully removed from the 96-well plate and mixed with iPSC-ECs, PCs, and ACs in fibrinogen at the ratios needed to generate the triculture BBB MVNs. An equal amount of thrombin was added and mixed with all the cells and spheroid prior to injecting into the devices for fibrin polymerization (85). Given prior validation that BBB microvessels self-assemble and stabilize within 7 d of culture (20, 69), we employed a similar timeline for the BBB-GBM model. Biological changes at the BBB are observed within 7 d and can be quantified near vs. far away from the tumor.

Tumor Growth, Vessel Coverage, and Vessel-Density Measurements. Tumor growth in the devices was measured daily between days 0 (seeding) and 7 by quantifying the GFP signal of the GBM spheroids using an Eclipse Ti epifluorescence microscope (Nikon) and the Fiji distribution of ImageJ (NIH) (87). At times, devices were treated daily, starting on day 3, with anti-VEGF (catalog no. AF357-SP, R&D Systems) at a concentration of 0.25 $\mu\text{g}/\text{mL}$, and tumor size was quantified as described above. Vessel density was computed as described (29) by using confocal microscopy (model FV-1200, Olympus) and staining for CD31 (catalog no. ab3245, Abcam) at predetermined ROIs: tumor center, proximal, and distal. These results were compared to prior results from our group using human umbilical vein EC MVNs and ovarian (Skov3) spheroids or A549 (lung) spheroids (29). Additional details are in *SI Appendix, Supplementary Materials and Methods*.

Immunostaining and Image Analysis. Devices were fixed, permeabilized, and blocked prior to staining. Protein visualization was achieved by staining the fixed devices with anti-CD31 (catalog no. ab3245, Abcam), anti-LRP1 (catalog no. sc-57351, Santa Cruz Biotechnology), and anti-ZO-1 (catalog no. 61-7300, ThermoFisher Scientific) at 1:200 in phosphate-buffered saline (PBS), overnight at 4 °C on a shaker. Secondary antibodies were used at 1:200 in PBS (568 goat anti-rabbit A-11011 or 633 goat anti-mouse A-21052, Invitrogen) and DAPI (D1306, Invitrogen) at 1:1,000. Additional staining details are in *SI Appendix, Supplementary Materials and Methods*. Images were acquired with a confocal laser-scanning microscope (pde; FV-1200, Olympus).

For *in vivo* samples, brains were formalin-fixed and paraffin-embedded before staining with CC-3 (CC3 Rabbit Mab, 1:800; catalog no. 9664L [D175], Cell Signaling Technology) and rabbit polymer secondary (Biocare Medical catalog no. RMR 622L). Quantification of CC3 staining was performed in QuPath version (v)0.2.3 (Queen's University, Belfast) using QuPath's build-in "Positive cell detection" (88) with three ROIs of the same size manually placed per tumor section.

Protein-Expression Analysis. Expression analysis of LRP1 was performed by using a Proteinsimple automatic western assay as described (85–90) after fixation with paraformaldehyde. Devices were separated from the glass coverslip by using a razor blade, and different regions of the MVNs in fibrin gel were collected: four ROIs in the control MVNs without GBM spheroids and in the MVNs with GBM spheroids, two ROIs near and two ROIs far from the spheroid; $n = 5$ or 6 devices were employed for each condition. Samples were incubated in lysis buffer comprising 10 mL of 1 \times buffer (catalog no. 9803S, Cell Signaling Technologies), 1 μL of Benzonase Nuclease (catalog no. E8263, Millipore Sigma), and one tablet of protease inhibitor mixture (catalog no. 11836170001, Millipore Sigma) and stored at -80 °C. LRP1 signal (catalog no. sc-57351, Santa Cruz Biotechnology) was normalized to CD31 (catalog no. ab32457, Abcam) or β -actin (catalog no. 926-42210, Li-Cor) by using Compass software v5.0. The output of this automatic Western assay is not a standard blot, but rather a chemiluminescence spectrum; representative uncropped raw data for LRP1 signal in one device are included in *SI Appendix, Fig. S1*.

Generation and Characterization of LbL-NPs With and Without CDDP. Fluorescent liposomes were generated by using thin-film hydration followed by extrusion, with additional details in *SI Appendix, Supplementary Materials and Methods*.

For CDDP-loaded liposomes, the film was rehydrated with a highly concentrated 8 mg/mL solution of CDDP in milliQ water at 80 °C prior to extrusion. Next, liposomes were fluorescently labeled through *N*-hydroxysuccinimide (NHS) ester coupling of sulfo-cyanine5 NHS ester dye (Lumiprobe) to 1,2-distearoyl-*sn*-glycero-3-phosphoethanolamine headgroups, according to the manufacturer's instructions. Excess dye and/or drug was removed via KrosFlo II tangential flow filtration (TFF) system (Repligen). See *SI Appendix, Supplementary Materials and Methods* for CDDP quantification techniques.

Fluorescent polystyrene cores with carboxylated surfaces were purchased from Invitrogen with diameters of 0.02 μm , 0.1 μm , and 0.5 μm . Layering was achieved by sequentially adding oppositely charged polyelectrolytes as described (91) with further details in *SI Appendix, Supplementary Materials and Methods*. AP2 was custom-synthesized by the Biopolymers and Proteomic Core Facility at the Massachusetts Institute of Technology with the sequence (K*)TFFYGGSRGKRNFK-TEEY, in which K* denotes modification of the N terminus with lysine-azide. Copper-based click chemistry was used to conjugate the azide-modified AP2 to the propargyl-modified PLD as described (38), and copper was removed via TFF.

The hydrodynamic size, polydispersity index, and surface potential (zeta) were monitored throughout synthesis and prior to downstream experiments by using dynamic light scattering and laser Doppler anemometry (Malvern ZS90 Particle Analyzer, $\lambda = 633$ nm, material/dispersant refractive index 1.590/1.330; Malvern). Negative-staining transmission electron microscopy (2100 Field Emission Electron Microscope, JEOL) with 1% phosphotungstic acid in water was utilized to further characterize CDDP-loaded liposomes and confirm the dynamic light-scattering data.

NP Association with Cells in Two-Dimensional Culture or Isolated Three-Dimensional Spheroids. NP association in cell lines was quantified by using flow cytometry (FACS LSR II with high throughput sampler, BD Biosciences) after incubation with NPs at a final concentration of 10 $\mu\text{g}/\text{mL}$ lipid in media for 24 h. After washing with PBS to remove unassociated NPs, cell suspensions were analyzed for Cy5 fluorescence by using a 640-nm laser and 670/30 filter. Structured illumination microscopy with image deconvolution was performed after the same NP incubation period and washing steps as for flow cytometry to determine the intracellular localization in GBM22 cells as described (92) using an Inverted $\times 71$ microscope (Olympus).

NP association in spheroids (without MVNs) was quantified by incubating the spheroids with 80 μL of 30 $\mu\text{g}/\text{mL}$ (with respect to lipid concentration) NP suspension (bare, pPLD, or AP2 NPs) for 12 min. Day 13 was chosen to ensure that the spheroids in three dimensions without MVNs were assessed at the same time as spheroids in the MVNs. Following NP incubation, spheroids were washed with PBS and placed on a glass coverslip for three-dimensional imaging with a confocal microscope (model FV-1200, Olympus). NP intensity into the spheroids of ~ 600 μm in diameter was quantified by averaging the intensity per location of four diametrical lines in the spheroid using the "Plot Profile" function of ImageJ.

In Vitro Permeability Assay in the BBB-GBM Model. To prevent dye leakage from the side channels, a monolayer of iPS-ECs was added to both media channels of the microfluidic device on day 4 following cell seeding (41). Permeability was measured between days 6 and 8 in the MVNs with and without tumor spheroids. We quantified permeability using four ROIs per device, ensuring that ROIs were selected at the center of the device, where diffusion of solutes/NPs from the media channels to the central gel is reduced. The MVN permeabilities to 10- and 40-kDa dextran, polystyrene NPs (bare, pPLD, and AP2), as well as liposome NPs (bare, pPLD, and AP2) were quantified following perfusion of 80- μL suspensions as described (41). Bare polystyrene NPs of different sizes were also employed to assess size-dependent transport across the in vitro BBB MVNs. Briefly, devices were imaged via confocal microscopy (model FV-1200, Olympus) at 12-min intervals in an environmental chamber maintained at 37 $^{\circ}\text{C}$ and 5% CO_2 . Following automatic thresholding and segmentation using the Fiji distribution of ImageJ, z-stack images were employed to generate a three-dimensional mask of the microvasculature (41). Analysis of NP or dextran transport across the BBB (with and without tumor spheroids) was performed as described (41).

CDDP NP Treatment In Vitro and Cell-Death Quantification. CDDP NPs were made fresh, and CDDP concentrations in each NP formulation were quantified prior to each experiment. BBB-GBM devices were treated daily with 6 μM free CDDP or CDDP NPs per day. Tumor size was measured over time as described above. Fluorescently labeled CDDP NPs with cyanine5 were used to quantify CDDP NP uptake in GBM tumors. To evaluate cell death, devices were incubated with 5 μM of Sytox Orange (catalog no. S11368, ThermoFisher Scientific) and DAPI for 1 h, applying a hydrostatic pressure drop across the gel channel (85). Confocal microscope images (FV-1200) were automatically thresholded and segmented by using the Fiji distribution of ImageJ, and z-stack images were employed to generate a three-dimensional mask of the GBM tumors to quantify Sytox signal inside and near the tumor (41).

Real-Time qRT-PCR. Gene expression was quantified via real-time qRT-PCR for BBB-GBM devices treated with free CDDP, bare CDDP NPs, or AP2 CDDP NPs using an RNeasy Mini Kit (catalog no. 74104, Qiagen) and the 7900HT Fast Real-Time PCR System using the TaqMan Fast Advanced Master Mix (catalog no. 4444556, Thermo Fisher Scientific) as described (69). Additional details are in *SI Appendix, Supplementary Materials and Methods*.

Intravital Imaging and Mouse Permeability Assay. For intravital imaging, NCR/nude mice (Taconic) were injected with fluorescent, functionalized liposomal NPs (100 μL via tail vein at a concentration of 0.5 mg/mL lipid in 5% dextrose), then anesthetized according to an IACUC-approved protocol. Immediately prior to cranial window surgery, mice were dosed with fluorescent dextran of varying molecular weights (100 μL via retro-orbital injection at a concentration of 2 mg/mL dextran). To create the cranial window, the skull was exposed, and a high-speed hand drill (Dremel) was used to thin the skull until the dura mater was exposed over the right frontal cortex. Multiphoton imaging was performed on an Olympus FV-1000MPE multiphoton microscope (Olympus) using a 25 \times , numerical aperture 1.05 objective. Excitation was achieved by using a femtosecond pulse laser at 840 nm, and emitted fluorescence was collected by photomultiplier tubes with emission filters of 425/30 nm for Collagen 1, 525/45 nm for fluorescein isothiocyanate-labeled dextran, and 672/30 nm for Cy5 NPs. Collagen 1 was excited by second harmonic generation and emitted as polarized light at half the excitation wavelength. The collagen 1 signal was used to identify the dura, such that the vessels imaged were within the cortex (50 to 100 μm below the dura; *SI Appendix, Fig. S5*). Images were acquired every 1 to 2 min for 10 to 20 min for analysis, as described below. Mice were maintained under anesthesia for the duration of the imaging and then humanely euthanized.

Acquired images from intravital imaging were then thresholded and segmented by using the Fiji distribution of ImageJ just as in the in vitro permeability workflow described above. Vessels below the dura and arteries were considered to ensure that these represent BBB capillaries in the mouse brain. The microvasculature filled with dextran (dextran channel) was employed to generate a three-dimensional mask of the BBB mouse vessels (Fig. 3A and *SI Appendix, Fig. S5*). This mask was employed to analyze both dextran and NP transport since dextran filled the entire vasculature and resulted in the most accurate mask of the three-dimensional vessels. After masking, analysis of NP or dextran transport was performed as described (41).

Vessel Dimensions. Acquired images from in vitro and in vivo samples perfused with fluorescent dextran were analyzed for vessel dimensions. Z-stack images were thresholded and segmented, and the built-in skeletonize function of Fiji was used to measure vessel dimensions as described (86).

Tumor Implantation and NP Treatment. For tumor implantation, we utilized a modified version of the intracranial xenograft protocol developed in the laboratory of Jann Sarkaria (22). In brief, NCR/nude mice (Taconic) were anesthetized with ketamine and xylazine and placed in a stereotactic head frame (Stoelting). Using sterile technique, the skull was exposed, and a small burr hole was made in the skull at coordinates 1 mm lateral and 2 mm posterior to Bregma. A total of 200,000 cells were injected 3 mm below the dura by using a 33-G 5- μL Neuro syringe (Hamilton Company) and Stoelting quintessential stereotaxic injector at a rate of 1 $\mu\text{L}/\text{min}$. Twelve days after tumor implantation, mice with confirmed intracranial tumors by MRI were randomized and treated with three doses of CDDP-containing NPs or free drug (0.75 mg CDDP/kg/dose). Control mice received empty control NPs with equivalent lipid to CDDP NP. All solutions were suspended in 5% dextrose and dosed via tail vein at 100 μL per injection.

MRI Methods and Tumor Volume Quantification. MRI was performed on a former Varian/Agilent 7T MRI operated by a Bruker AV4 NeoBioSpec70-20USR console, equipped with a Bruker QSN075/040 radiofrequency coil. Mice were anesthetized with isoflurane throughout, according to approved IACUC protocol. Data were collected and reconstructed within Bruker Paravision PV360 v2.0. T2 weighted images were obtained by using TurboRARE sequence with the following parameters: axial orientation, repetition time/echo time = 3,000/25 ms, 256 \times 256 matrix, field of view = 20 \times 20 mm^2 , interleaved number of slices = 32, no gap and slice thickness = 0.5 mm, number of averages = 4, and rapid acquisition with relaxation enhancement (RARE) factor 8. Images were converted to DICOM format.

MRI images were analyzed by using the Fiji distribution of ImageJ using a published method for diameter-based measurement (93). Using the native images obtained in the coronal plane, the z-slice with maximum craniocaudal (d_{cc}) and lateral (d_l) dimensions was determined, and these diameters recorded. An axial reconstruction was then generated by using the built-in "Reslice" function in Fiji with output spacing of 0.5 mm (z-slice distance), creating a 40-slice axial image. Using axial images, the slice with maximal anteroposterior diameter

(d_{ap}) was determined. The diameter-based volume (V) was then computed by using the ellipsoid formula ($V = d_{cc} \times d_l \times d_{ap} \times \pi/6$). On MRI, some mice were noted to have small subcutaneous collections consistent with tumor cell extravasation from the burr hole. In these cases, tumors were only considered evaluable if there was a clear and distinct intracranial component and were excluded from all analyses otherwise.

Statistical Analysis. All data are plotted as mean \pm SD, unless indicated otherwise. Statistical significance was assessed by using Student's t tests when comparing two conditions/groups, one-way ANOVA with Tukey's honestly significant difference post hoc test when comparing more than two groups, or Kruskal-Wallis multiple comparison test (when applicable) with the software Prism (GraphPad). For nonhomogeneity of variances, as determined via Levene's test, Brown-Forsythe and Welch ANOVA with Dunnett's T3 post hoc test was performed with the software Prism. Results were represented as follows: ns stands for not significant; $*P < 0.05$; $**P < 0.01$; $***P < 0.001$; and $****P < 0.0001$. In all in vitro experiments, six to eight devices per condition were employed, unless otherwise indicated. In all in vivo mice experiments, three to seven mice per condition were used unless otherwise indicated.

Data Availability. All study data are included in the article and/or the supporting information.

1. Q. T. Ostrom *et al.*, CBRUS statistical report: Primary brain and other central nervous system tumors diagnosed in the United States in 2012-2016. *Neuro-Oncol.* **21** (suppl. 5), v1-v100 (2019).
2. Q. T. Ostrom, D. J. Cote, M. Ascha, C. Kruchko, J. S. Barnholtz-Sloan, Adult glioma incidence and survival by race or ethnicity in the United States from 2000 to 2014. *JAMA Oncol.* **4**, 1254-1262 (2018).
3. M. Glas *et al.*, Residual tumor cells are unique cellular targets in glioblastoma. *Ann. Neurol.* **68**, 264-269 (2010).
4. R. Stupp *et al.*; European Organisation for Research and Treatment of Cancer Brain Tumor and Radiotherapy Groups; National Cancer Institute of Canada Clinical Trials Group, Radiotherapy plus concomitant and adjuvant temozolomide for glioblastoma. *N. Engl. J. Med.* **352**, 987-996 (2005).
5. N. J. Abbott, A. A. Pata Bendige, D. E. Dolman, S. R. Yusuf, D. J. Begley, Structure and function of the blood-brain barrier. *Neurobiol. Dis.* **37**, 13-25 (2010).
6. N. J. Abbott, L. Rönnbäck, E. Hansson, Astrocyte-endothelial interactions at the blood-brain barrier. *Nat. Rev. Neurosci.* **7**, 41-53 (2006).
7. C. Hajal, M. Campisi, C. Mattu, V. Chiono, R. D. Kamm, In vitro models of molecular and nanoparticle transport across the blood-brain barrier. *Biomicrofluidics* **12**, 042213 (2018).
8. D. S. Hersh *et al.*, Evolving drug delivery strategies to overcome the blood brain barrier. *Curr. Pharm. Des.* **22**, 1177-1193 (2016).
9. L. L. Muldoon *et al.*, Chemotherapy delivery issues in central nervous system malignancy: A reality check. *J. Clin. Oncol.* **25**, 2295-2305 (2007).
10. R. K. Oberoi *et al.*, Strategies to improve delivery of anticancer drugs across the blood-brain barrier to treat glioblastoma. *Neuro-Oncol.* **18**, 27-36 (2016).
11. M. Touat, A. Idhah, M. Sanson, K. L. Ligon, Glioblastoma targeted therapy: Updated approaches from recent biological insights. *Ann. Oncol.* **28**, 1457-1472 (2017).
12. C. D. Arvanitis, G. B. Ferraro, R. K. Jain, The blood-brain barrier and blood-tumour barrier in brain tumours and metastases. *Nat. Rev. Cancer* **20**, 26-41 (2020).
13. Y. Zhou, Z. Peng, E. S. Seven, R. M. Leblanc, Crossing the blood-brain barrier with nanoparticles. *J. Control. Release* **270**, 290-303 (2018).
14. C. Ferraris, R. Cavalli, P. P. Panciani, L. Battaglia, Overcoming the blood-brain barrier: Successes and challenges in developing nanoparticle-mediated drug delivery systems for the treatment of brain tumours. *Int. J. Nanomedicine* **15**, 2999-3022 (2020).
15. D. Bobo, K. J. Robinson, J. Islam, K. J. Thurecht, S. R. Corrie, Nanoparticle-based medicines: A review of FDA-approved materials and clinical trials to date. *Pharm. Res.* **33**, 2373-2387 (2016).
16. E. C. Dreaden *et al.*, Tumor-targeted synergistic blockade of MAPK and PI3K from a layer-by-layer nanoparticle. *Clin. Cancer Res.* **21**, 4410-4419 (2015).
17. L. Gu, Z. J. Deng, S. Roy, P. T. Hammond, A combination RNAi-chemotherapy layer-by-layer nanoparticle for systemic targeting of KRAS/P53 with cisplatin to treat non-small cell lung cancer. *Clin. Cancer Res.* **23**, 7312-7323 (2017).
18. F. C. Lam *et al.*, Enhanced efficacy of combined temozolomide and bromodomain inhibitor therapy for gliomas using targeted nanoparticles. *Nat. Commun.* **9**, 1991 (2018).
19. K. Boyé *et al.*, The role of CXCR3/LRP1 cross-talk in the invasion of primary brain tumors. *Nat. Commun.* **8**, 1571 (2017).
20. M. Campisi *et al.*, 3D self-organized microvascular model of the human blood-brain barrier with endothelial cells, pericytes and astrocytes. *Biomaterials* **180**, 117-129 (2018).
21. C. Hajal *et al.*, Engineered human blood-brain barrier microfluidic model for vascular permeability analyses. *Nat. Protoc.* **17**, 95-128 (2022).
22. B. L. Carlson, J. L. Pokorny, M. A. Schroeder, J. N. Sarkaria, Establishment, maintenance and in vitro and in vivo applications of primary human glioblastoma multiforme (GBM) xenograft models for translational biology studies and drug discovery. *Curr. Protoc. Pharmacol.* **Chapter 14**, Unit 14.16 (2011).
23. R. A. Vaubel *et al.*, Genomic and phenotypic characterization of a broad panel of patient-derived xenografts reflects the diversity of glioblastoma. *Clin. Cancer Res.* **26**, 1094-1104 (2020).
24. J. L. Pokorny *et al.*, The efficacy of the Wee1 inhibitor MK-1775 combined with temozolomide is limited by heterogeneous distribution across the blood-brain barrier in glioblastoma. *Clin. Cancer Res.* **21**, 1916-1924 (2015).
25. G. J. Kitange *et al.*, Inhibition of histone deacetylation potentiates the evolution of acquired temozolomide resistance linked to MGMT upregulation in glioblastoma xenografts. *Clin. Cancer Res.* **18**, 4070-4079 (2012).

ACKNOWLEDGMENTS. We thank the Koch Institute's Robert A. Swanson (1969) Biotechnology Center (supported by National Cancer Institute Grant P30-CA14051) for technical support, specifically the Microscopy Core Facility; the Hope Babette Tang (1983) Histology Core Facility; the Peterson (1957) Nanotechnology Materials Core Facility; the Flow Cytometry Core Facility; the Preclinical Modeling, Imaging & Testing Core Facility; and the Biopolymers & Proteomics Core Facility. Figs. 1, 3, and 5 were created in part with [BioRender.com](https://www.biorender.com). We also thank all members of the R.D.K. and P.T.H. laboratories for helpful discussions while developing this work.

Author affiliations: ^aKoch Institute for Integrative Cancer Research, Massachusetts Institute of Technology, Cambridge, MA 02139; ^bDepartment of Pediatric Oncology, Dana-Farber Cancer Institute, Boston, MA 02115; ^cDivision of Pediatric Hematology/Oncology, Boston Children's Hospital, Boston, MA 02115; ^dDepartment of Mechanical Engineering, Massachusetts Institute of Technology, Cambridge, MA 02139; ^eDepartment of Biological Engineering, Massachusetts Institute of Technology, Cambridge, MA 02139; ^fCenter for Research in Molecular Medicine and Chronic Diseases, Universidade de Santiago de Compostela, 15705 Santiago de Compostela, Spain; and ^gDepartment of Chemical Engineering, Massachusetts Institute of Technology, Cambridge, MA 02139

Author contributions: J.P.S., C.H., R.D.K., and P.T.H. designed research; J.P.S., C.H., H.C.S., and J.W. performed research; G.S.O., N.B., and T.G.D. contributed new reagents/analytic tools; J.P.S., C.H., H.C.S., and G.S.O. analyzed data; and J.P.S., C.H., R.D.K., and P.T.H. wrote the paper.

Reviewers: B.H., University of Illinois Urbana-Champaign; S.M., Harvard University; and R.S.-F., Tel Aviv University.

26. Y. Nashimoto *et al.*, Vascularized cancer on a chip: The effect of perfusion on growth and drug delivery of tumor spheroid. *Biomaterials* **229**, 119547 (2020).
27. G. J. Baker *et al.*, Mechanisms of glioma formation: Iterative perivascular glioma growth and invasion leads to tumor progression, VEGF-independent vascularization, and resistance to antiangiogenic therapy. *Neoplasia* **16**, 543-561 (2014).
28. E. A. Kuczynski, P. B. Vermeulen, F. Pezella, R. S. Kerbel, A. R. Reynolds, Vessel co-option in cancer. *Nat. Rev. Clin. Oncol.* **16**, 469-493 (2019).
29. K. Haase, G. S. Offeddu, M. R. Gillrie, R. D. Kamm, Endothelial regulation of drug transport in a 3D vascularized tumor model. *Adv. Funct. Mater.* **30**, 2002444 (2020).
30. J. N. Sarkaria *et al.*, Is the blood-brain barrier really disrupted in all glioblastomas? A critical assessment of existing clinical data. *Neuro-oncol.* **20**, 184-191 (2018).
31. E. K. Nduom, C. Yang, M. J. Merrill, Z. Zhuang, R. R. Lonser, Characterization of the blood-brain barrier of metastatic and primary malignant neoplasms. *J. Neurosurg.* **119**, 427-433 (2013).
32. L. G. Dubois *et al.*, Gliomas and the vascular fragility of the blood brain barrier. *Front. Cell. Neurosci.* **8**, 418 (2014).
33. S. L. Gonias, W. M. Campana, LDL receptor-related protein-1: A regulator of inflammation in atherosclerosis, cancer, and injury to the nervous system. *Am. J. Pathol.* **184**, 18-27 (2014).
34. M. Demeule *et al.*, Involvement of the low-density lipoprotein receptor-related protein in the transcytosis of the brain delivery vector angiopep-2. *J. Neurochem.* **106**, 1534-1544 (2008).
35. C. Ché *et al.*, New angiopep-modified doxorubicin (ANG1007) and etoposide (ANG1009) chemotherapeutics with increased brain penetration. *J. Med. Chem.* **53**, 2814-2824 (2010).
36. Y. Bertrand *et al.*, Influence of glioma tumour microenvironment on the transport of ANG1005 via low-density lipoprotein receptor-related protein 1. *Br. J. Cancer* **105**, 1697-1707 (2011).
37. X. Ji, H. Wang, Y. Chen, J. Zhou, Y. Liu, Recombinant expressing angioep-2 fused anti-VEGF single chain Fab (scFab) could cross blood-brain barrier and target glioma. *AMB Express* **9**, 165 (2019).
38. N. Boehnke *et al.*, Theranostic layer-by-layer nanoparticles for simultaneous tumor detection and gene silencing. *Angew. Chem. Int. Ed. Engl.* **59**, 2776-2783 (2020).
39. S. Correa, E. C. Dreaden, L. Gu, P. T. Hammond, Engineering nanolayered particles for modular drug delivery. *J. Control. Release* **240**, 364-386 (2016).
40. M. Demeule *et al.*, Identification and design of peptides as a new drug delivery system for the brain. *J. Pharmacol. Exp. Ther.* **324**, 1064-1072 (2008).
41. G. S. Offeddu *et al.*, An on-chip model of protein paracellular and transcellular permeability in the microcirculation. *Biomaterials* **212**, 115-125 (2019).
42. G. S. Offeddu *et al.*, Application of transmural flow across in vitro microvasculature enables direct sampling of interstitial therapeutic molecule distribution. *Small* **15**, e1902393 (2019).
43. X. Liang, G. Mao, K. Y. Ng, Mechanical properties and stability measurement of cholesterol-containing liposome on mica by atomic force microscopy. *J. Colloid Interface Sci.* **278**, 53-62 (2004).
44. D. Guo, J. Li, G. Xie, Y. Wang, J. Luo, Elastic properties of polystyrene nanospheres evaluated with atomic force microscopy: Size effect and error analysis. *Langmuir* **30**, 7206-7212 (2014).
45. R. Hartmann, M. Weidenbach, M. Neubauer, A. Fery, W. J. Parak, Stiffness-dependent in vitro uptake and lysosomal acidification of colloidal particles. *Angew. Chem. Int. Ed. Engl.* **54**, 1365-1368 (2015).
46. L. Ribovski *et al.*, Low nanogel stiffness favors nanogel transcytosis across an in vitro blood-brain barrier. *Nanomedicine (Lond.)* **34**, 102377 (2021).
47. P. Guo *et al.*, Nanoparticle elasticity directs tumor uptake. *Nat. Commun.* **9**, 130 (2018).
48. Y. Bertrand *et al.*, Transport characteristics of a novel peptide platform for CNS therapeutics. *J. Cell. Mol. Med.* **14**, 2827-2839 (2010).
49. I. Canton, G. Battaglia, Endocytosis at the nanoscale. *Chem. Soc. Rev.* **41**, 2718-2739 (2012).
50. B. Oller-Salvia, M. Sánchez-Navarro, E. Giral, M. Teixidó, Blood-brain barrier shuttle peptides: An emerging paradigm for brain delivery. *Chem. Soc. Rev.* **45**, 4690-4707 (2016).
51. S. Sindhwani *et al.*, The entry of nanoparticles into solid tumours. *Nat. Mater.* **19**, 566-575 (2020).
52. W. Wick, A. Wick, M. Weiler, M. Weller, Patterns of progression in malignant glioma following anti-VEGF therapy: Perceptions and evidence. *Curr. Neurol. Neurosci. Rep.* **11**, 305-312 (2011).
53. W. Yuan, Y. Lv, M. Zeng, B. M. Fu, Non-invasive measurement of solute permeability in cerebral microvessels of the rat. *Microvasc. Res.* **77**, 166-173 (2009).

54. N. Kutuzov, H. Flyvbjerg, M. Lauritzen, Contributions of the glycocalyx, endothelium, and extravascular compartment to the blood-brain barrier. *Proc. Natl. Acad. Sci. U.S.A.* **115**, E9429–E9438 (2018).
55. M. Patrizi, M. Bartucci, S. R. Pine, H. E. Sabaawy, Utility of glioblastoma patient-derived orthotopic xenografts in drug discovery and personalized therapy. *Front. Oncol.* **8**, 23 (2018).
56. T. J. Brown *et al.*, Association of the extent of resection with survival in glioblastoma: A systematic review and meta-analysis. *JAMA Oncol.* **2**, 1460–1469 (2016).
57. M. Rapp *et al.*, Recurrence pattern analysis of primary glioblastoma. *World Neurosurg.* **103**, 733–740 (2017).
58. A. B. Nair, S. Jacob, A simple practice guide for dose conversion between animals and human. *J. Basic Clin. Pharm.* **7**, 27–31 (2016).
59. J. C. Buckner *et al.*; North Central Cancer Treatment Group 93-72-52; Southwest Oncology Group 9503 Trials, Phase III trial of carmustine and cisplatin compared with carmustine alone and standard radiation therapy or accelerated radiation therapy in patients with glioblastoma multiforme: North Central Cancer Treatment Group 93-72-52 and Southwest Oncology Group 9503 trials. *J. Clin. Oncol.* **24**, 3871–3879 (2006).
60. S. Pozzi *et al.*, Meet me halfway: Are in vitro 3D cancer models on the way to replace in vivo models for nanomedicine development? *Adv. Drug Deliv. Rev.* **175**, 113760 (2021).
61. D. Sood *et al.*, 3D extracellular matrix microenvironment in bioengineered tissue models of primary pediatric and adult brain tumors. *Nat. Commun.* **10**, 4529 (2019).
62. T. J. DePalma, H. Sivakumar, A. Skardal, Strategies for developing complex multi-component in vitro tumor models: Highlights in glioblastoma. *Adv. Drug Deliv. Rev.* **180**, 114067 (2022).
63. X. Wang *et al.*, Reciprocal signaling between glioblastoma stem cells and differentiated tumor cells promotes malignant progression. *Cell Stem Cell* **22**, 514–528.e5 (2018).
64. W. Diao *et al.*, Behaviors of glioblastoma cells in in vitro microenvironments. *Sci. Rep.* **9**, 85 (2019).
65. M. T. Ngo, B. A. Harley, The influence of hyaluronic acid and glioblastoma cell coculture on the formation of endothelial cell networks in gelatin hydrogels. *Adv. Healthc. Mater.*, 10.1002/adhm.201700687 (2017).
66. H. Xu *et al.*, A dynamic in vivo-like organotypic blood-brain barrier model to probe metastatic brain tumors. *Sci. Rep.* **6**, 36670 (2016).
67. M. S. Ozturk *et al.*, High-resolution tomographic analysis of in vitro 3D glioblastoma tumor model under long-term drug treatment. *Sci. Adv.* **6**, eaay7513 (2020).
68. A. Linkous *et al.*, Modeling patient-derived glioblastoma with cerebral organoids. *Cell Rep.* **26**, 3203–3211.e5 (2019).
69. C. Hajal *et al.*, The CCL2-CCR2 astrocyte-cancer cell axis in tumor extravasation at the brain. *Sci. Adv.* **7**, eabg8139 (2021).
70. F. Winkler *et al.*, Imaging glioma cell invasion in vivo reveals mechanisms of dissemination and peritumoral angiogenesis. *Glia* **57**, 1306–1315 (2009).
71. C. Hajal, B. Le Roi, R. D. Kamm, B. M. Maoz, Biology and models of the blood-brain barrier. *Annu. Rev. Biomed. Eng.* **23**, 359–384 (2021).
72. C. Hajal, L. Ibrahim, J. C. Serrano, G. S. Offeddu, R. D. Kamm, The effects of luminal and trans-endothelial fluid flows on the extravasation and tissue invasion of tumor cells in a 3D in vitro microvascular platform. *Biomaterials* **265**, 120470 (2021).
73. G. S. Offeddu *et al.*, Microheart: A microfluidic pump for functional vascular culture in microphysiological systems. *J. Biomech.* **119**, 110330 (2021).
74. P. T. Ronaldson, T. P. Davis, Regulation of blood-brain barrier integrity by microglia in health and disease: A therapeutic opportunity. *J. Cereb. Blood Flow Metab.* **40**(1_suppl), S6–S24 (2020).
75. T. L. Moore *et al.*, Nanoparticle administration method in cell culture alters particle-cell interaction. *Sci. Rep.* **9**, 900 (2019).
76. L. Shi, M. Zeng, Y. Sun, B. M. Fu, Quantification of blood-brain barrier solute permeability and brain transport by multiphoton microscopy. *J. Biomech. Eng.* **136**, 031005 (2014).
77. W. Zhang *et al.*, Differential expression of receptors mediating receptor-mediated transcytosis (RMT) in brain microvessels, brain parenchyma and peripheral tissues of the mouse and the human. *Fluids Barriers CNS* **17**, 47 (2020).
78. M. E. Berens, A. Giese, "...those left behind." Biology and oncology of invasive glioma cells. *Neoplasia* **1**, 208–219 (1999).
79. T. Hara *et al.*, Interactions between cancer cells and immune cells drive transitions to mesenchymal-like states in glioblastoma. *Cancer Cell* **39**, 779–792.e11 (2021).
80. R. J. Shannon, K. L. Carpenter, M. R. Guilfoyle, A. Helmy, P. J. Hutchinson, Cerebral microdialysis in clinical studies of drugs: Pharmacokinetic applications. *J. Pharmacokinet. Pharmacodyn.* **40**, 343–358 (2013).
81. C. D. Edington *et al.*, Interconnected microphysiological systems for quantitative biology and pharmacology studies. *Sci. Rep.* **8**, 4530 (2018).
82. A. Herland *et al.*, Quantitative prediction of human pharmacokinetic responses to drugs via fluidically coupled vascularized organ chips. *Nat. Biomed. Eng.* **4**, 421–436 (2020).
83. M. Trapecar *et al.*, Human physiometric model integrating microphysiological systems of the gut, liver, and brain for studies of neurodegenerative diseases. *Sci. Adv.* **7**, eabd1707 (2021).
84. R. Novak *et al.*, Robotic fluidic coupling and interrogation of multiple vascularized organ chips. *Nat. Biomed. Eng.* **4**, 407–420 (2020).
85. M. B. Chen *et al.*, Inflamed neutrophils sequestered at entrapped tumor cells via chemotactic confinement promote tumor cell extravasation. *Proc. Natl. Acad. Sci. U.S.A.* **115**, 7022–7027 (2018).
86. K. Haase, M. R. Gillrie, C. Hajal, R. D. Kamm, Pericytes contribute to dysfunction in a human 3D model of placental microvasculature through VEGF-Ang-Tie2 signaling. *Adv. Sci. (Weinh.)* **6**, 1900878 (2019).
87. J. Schindelin *et al.*, Fiji: An open-source platform for biological-image analysis. *Nat. Methods* **9**, 676–682 (2012).
88. P. Bankhead *et al.*, QuPath: Open source software for digital pathology image analysis. *Sci. Rep.* **7**, 16878 (2017).
89. G. S. Offeddu *et al.*, The cancer glycocalyx mediates intravascular adhesion and extravasation during metastatic dissemination. *Commun. Biol.* **4**, 255 (2021).
90. G. Offeddu *et al.*, Glycocalyx-mediated vascular dissemination of circulating tumor cells. bioRxiv [Preprint] (2020). <https://doi.org/10.1101/2020.04.28.066746> (Accessed 25 April 2022).
91. S. Correa *et al.*, Highly scalable, closed-loop synthesis of drug-loaded, layer-by-layer nanoparticles. *Adv. Funct. Mater.* **26**, 991–1003 (2016).
92. N. Boehnke, K. J. Dolph, V. M. Juarez, J. M. Lanoha, P. T. Hammond, Electrostatic conjugation of nanoparticle surfaces with functional peptide motifs. *Bioconjug. Chem.* **31**, 2211–2219 (2020).
93. H. J. Kim, W. Kim, Method of tumor volume evaluation using magnetic resonance imaging for outcome prediction in cervical cancer treated with concurrent chemotherapy and radiotherapy. *Radiat. Oncol. J.* **30**, 70–77 (2012).